Construction and Building Materials 304 (2021) 124635

Contents lists available at ScienceDirect

Construction and Building Materials

journal homepage: www.elsevier.com/locate/conbuildmat

Characteristics of new cement-based thermoelectric composites for low-temperature applications

Xiaoli Liu [a], Ming Qu [a,*], Alan Phong Tran Nguyen [b], Neil R. Dilley [c], Kazuaki Yazawa [c]

[a] Lyles School of Civil Engineering, Purdue University, West Lafayette, IN 47907, USA
[b] School of Mechanical Engineering, Purdue University, West Lafayette, IN 47907, USA
[c] Birck Nanotechnology Center, Purdue University, West Lafayette, IN 47907, USA

ARTICLE INFO

Keywords:
Thermoelectric cement composite
Thermal conductivity
Electrical conductivity
Seebeck coefficient
Figure of merit

ABSTRACT

Thermoelectric cement, the mixture of cement and thermoelectric additives, can convert energy between thermal and electrical forms due to the thermoelectric additives. Potentially, they could be the material for building envelopes to harvest waste heat and/or provide space cooling or heating. When there is a significant difference between indoor and outdoor temperatures, the thermoelectric cement can generate electricity using the temperature gradient. And the same material can cool or heat building space via building envelopes with an electrical input. The research aimed to identify and characterize thermoelectric cement candidates for building envelope applications. The additives used in the studied thermoelectric cement candidates include graphite and MnO_2. Except for the additives, the study also explored the impact of the two different fabrication methods: wet-mixing and dry-mixing on thermoelectric performance. The images of TE cement candidates taken by scanning electron microscopy and energy dispersive X-ray microscopy visualized the morphology and distribution of additives in the thermoelectric cement composites. The DynaCool Physical Properties Measurement System used in the study simultaneously measured the candidates' thermoelectric properties, including thermal conductivity, electrical conductivity, Seebeck coefficient, and Figure of merit (*ZT*). The test results showed that the thermoelectric cement with the additives of 10% (weight ratio) graphite and 5% MnO_2 has the highest *ZT* of 6.2×10^{-6} at 350 K. *ZT* of the thermoelectric cement is even higher to 10^{-5} orders of magnitude when applying a four-probe electrical resistivity method to account for the contact resistance.

1. Introduction

Economic growth requires more energy, but unreasonable energy use will cause ecological imbalances and threaten the living environment for human beings. Therefore, utilizing renewable and clean energy and improving energy efficiency have become measures to break this vicious circle. Thermoelectric (TE) technology is one good measure. TE technology can convert energy between thermal and electrical forms. Recently, researchers have applied TE materials to the pavements and building envelopes to harvest waste heat. In hot summer, the exterior surface (possibly exceeding 60 °C) will aggravate the urban heat island effect. Researchers integrated conventional Bi_2Te_3-based TE modules in the pavement to generate electricity by using the temperature difference between the two surfaces of pavement, and also it could cool the road [1–5]. The TE modules have also been applied to building envelopes [6–11] to provide cooling or heating power for a building by using electricity from solar photovoltaic panels. The energy conversion via TE modules in buildings has high flexibility, scalability, reliability, and no harmful effect during operation [12]. The current testing prototypes of the TE building envelope use commercially available TE modules aimed at small component applications like computer CPUs. They have a low heat dissipation rate and are inapplicable in buildings. Therefore, TE cement composites could be a better choice than TE modules because of the high integrity and low cost of TE-cement building envelopes [13].

A competitive TE cement needs to have high TE performances, indicated by the power factor (*PF*) and the dimensionless Figure of merit (*ZT*). A higher *PF* indicates the TE material's higher power generation capacity when it works as a power generator. A high *ZT* means a better coefficient of performance of a TE component when it works as a heat pump. *ZT* is determined by three intrinsic material properties: Seebeck coefficient, electrical conductivity, and thermal conductivity. A higher Seebeck coefficient, a higher electrical conductivity, and a lower

* Corresponding author at: Civil Engineering Building, 550 Stadium Mall Drive, West Lafayette, IN 47907-2051, USA.
E-mail address: mqu@purdue.edu (M. Qu).

https://doi.org/10.1016/j.conbuildmat.2021.124635
Received 23 November 2020; Received in revised form 17 August 2021; Accepted 19 August 2021
Available online 27 August 2021

thermal conductivity lead to a higher ZT value. The additives to cement play a critical role in the TE performances of TE cement. However, no model exists to guide the selection of additives for higher performance. Researchers have investigated different additives experimentally. Among these studies, most of them reported the Seebeck coefficient and the electrical conductivity. Still, few of them measured the thermal conductivity and published the *ZT* values. Fig. 1 summarizes the four TE properties of the TE cement published according to the additives, including carbon fiber, graphene, carbon nanotubes (CNT), steel fiber, metallic oxides, and the mixture of the doped metallic oxides and graphene. As shown, for carbon fiber enhanced TE cement, the Seebeck coefficient of the TE cement is at the range of 5.44–22.07 μV/K [14,15] except for the highest value of 127 μV/K reported by Bahar and Salih [16]. Their electrical conductivity was 0.2 S/m, comparable with semiconductors. The overall *ZT* of carbon fiber enhanced TE cement was about 1.33×10^{-7} at 27 °C [17].

Graphite or graphene as additives can significantly increase electrical conductivity up to 2480 S/m (expanded graphite [18]) and 1168 S/m (graphene [19]), leading to a high *ZT* of 6.8×10^{-4} and 4.4×10^{-4}, respectively. However, their Seebeck coefficients were consistently lower than 34 μV/K due to zero bandgap of graphite. In 2020, Ghosh et al. added Aluminum doped ZnO powders to graphene-enhanced TE cement. They reported the *ZT* for TE cement as 1.01×10^{-2} at around 70 °C [20], the highest *ZT* value of the TE cement published. For CNT, Wei et al. [21] reported a potentially higher electrical conductivity by using dry mixing and compression. Tzounis et al. [22] doped carbon nanotubes and fabricated both n-type and p-type CNT-enhanced cement. The Seebeck coefficients of the n-type and p-type were around −58 μV/K and +20 μV/K, respectively.

As observed, 1% steel-fiber enhanced concrete has exhibited a negative Seebeck coefficient of −64 μV/K [23], while 3% $Ca_3Co_4O_9$ powder increased the Seebeck coefficient to 58.6 μV/K at room temperature [24]. The Seebeck coefficient of cement with 5% Bi_2O_3 was +100 μV/K [25]. Ji et al. [26] subsequently synthesized a TE cement composite with a significant Seebeck coefficient over 1000 μV/K, using ZnO, Fe_2O_3, and MnO_2 powder enhanced materials. However, Ghahari et al. [27] tested cement slurry with ZnO nanoparticles and showed a maximum Seebeck coefficient of only 0.16–0.185 μV/K. According to the literature review, several observations are as follows.

The additives with the most potential for *ZT* improvements are graphene and metallic oxides. Graphene or expanded graphite increases electrical conductivity while metal oxides such as AZO and MnO_2 improve the Seebeck coefficient. The combination of graphite and metallic oxides could further improve TE performance.

Before 2014, most characterization studies focused on the Seebeck coefficient measurement [14–16,24,25,28] only. However, the Seebeck coefficient is not the single indicator for TE performance. The overall performance of TE materials should also include other parameters such as *ZT*, an indicator of the heat pumping performance of TE. Therefore, the thermal conductivity, electrical conductivity, and Seebeck coefficient need to be measured to evaluate the TE performance in energy generation and heat pumping.

The challenge in the TE material characterization is how to measure the TE properties accurately. The published studies did not measure the TE properties simultaneously. The difference in the operating conditions, sizes, concentrations, and distribution of additives in different samples can affect TE performance measurement. Hence, the *ZT,* the product of the square of the Seebeck coefficient and the ratio between electrical conductivity and thermal conductivity, may not be accurate.

Therefore, the study aims to address these challenges by identifying the new TE cement and characterizing them accurately. According to the literature, surface-enhanced flake graphite (SEFG) and MnO_2 enhanced cement composites were selected as the new TE cement composite. Since the mixing method of the cement has influenced the TE performance, the study also investigated the impact of two mixing ways on the TE cement. The morphology, concentration, and distribution of various elements in the samples were identified using the scanning electron microscope (SEM) and the energy-dispersive X-ray spectroscopy (EDX) techniques. The DynaCool Physical Properties Measurement System (PPMS) was used to measure the Seebeck coefficient, thermal conductivity, and electrical conductivity of the samples simultaneously at different temperatures. The measurements of the parameters were used to evaluate the ZT values of the tested samples.

The paper includes four sections. Section 2 is the experimental methods, including material preparation, fabrication of specimens, characterization techniques, and uncertainty analysis. Section 3 presents SEM and EDX images and TE parameters measured. Finally, Section 4 is the conclusion.

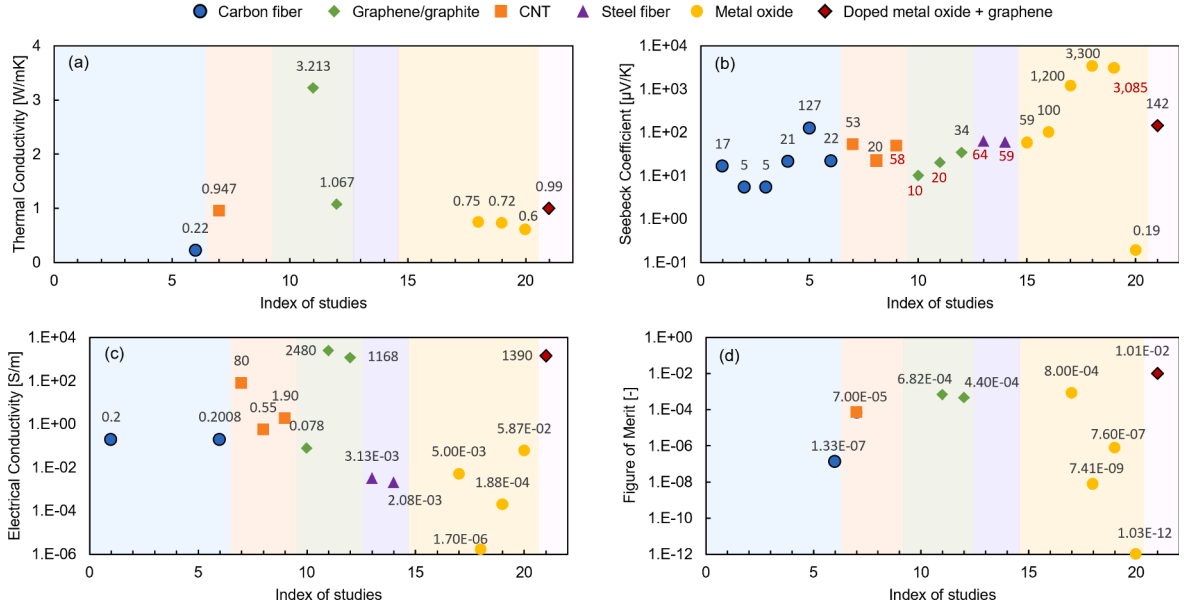

Fig. 1. The historical data of TE transport properties for different TE cement published in the literature from 1998 to 2020: (a) thermal conductivity, (b) Seebeck coefficient, (c) electrical conductivity, and (d) Figure of merit.

2. Methodology

2.1. Material preparation

Portland cement (Type-III), purchased from Buzzi Unicem USA, was used in this research. With the same composition as the Type-I cement, a smaller cement particle size of Type III cement allows even distribution of all particles (average particle size less than 10 μm [29]). The Surface Enhanced Flake Graphite (SEFG, grade 3775), purchased from Asbury Graphite Mills, Inc, USA, is a highly lightweight material manufactured by heating expandable graphite under high temperatures to expand its molecular structure and then compressing into particles with the flake morphology. The SEFG has a specific surface area as high as 27 m^2/g and a size of 8 μm. The concentrations of SEFG employed were in amounts of 5, 10, 15 wt% by mass of cement in cement composites (CC), which were subsequently labeled 5SEFG/CC, 10SEFG/CC, and 15SEFG/CC. The nanoparticles of manganese dioxides (MnO_2), purchased from US Research Nanomaterials, Inc, USA, have an average diameter of 50 nm, a purity of 98%, and a density of 5.02 g/cm^3. The concentration of MnO_2 nanopowder used was 5% by mass of the cement, and its mixture with 10% SEFG was labeled 5 MnO_2-10SEFG/CC. There was no other aggregate.

2.2. Specimen fabrication

This research used two mixing methods: dry-mixing and wet-mixing (conventional method) to prepare composite samples. Schematic diagrams of the sample preparation by the dry-mixing and wet-mixing are shown in Fig. 2(a)-(c) and Fig. 2(d)-(f), respectively.

In the dry-mixing, the cement powder and additives were mixed without water and dispersant use. An even distribution of the mixture was obtained when the color of the dry mix became uniformly grey. Then, the homogeneous mixture was placed in a customized cylindrical stainless-steel mold with a metal strip and a die block. A mechanical test system (MTS) applied the pressure at 50 MPa to the metal strip, which compressed the dry mixture into a cylinder with a diameter of 9.5 mm (3/8 in.) and a height of 5 ~ 10 mm shown in Fig. 3. The compact cylinder sample was first put on a saturated sponge for 24 h to pre-cure, and it was next soaked in water for three days to be fully cured. After curing, the sample was placed in the lab under a steady condition of 25 °C and relative humidity of 50%.

In the wet-mixing, the additives were first dissolved into a solution of water reducer and water. The amounts of water reducer and water were 0.6 wt% and 40 wt% of the cement, respectively. The wet mixture was mixed with the cement powder and poured into a customized resin mold for 24 h in the ambient atmosphere. The 10 × 10 × 5 mm^3 samples were then removed from the mold and placed in a curing chamber at 28 °C and relative humidity of 100% for three days. Finally, the samples prepared by both methods were ground to cuboids of a similar size with a cross-sectional area of 5 × 5 mm^2 and a thickness of 5 ~ 10 mm to reduce the size variation.

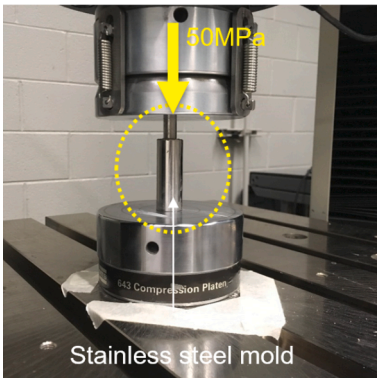

Fig. 3. The dry compression method using a mechanical test system.

The dry-mixing applied a high compression on mixing composite materials with much less water and fewer voids than the wet-mixing. Fig. 4 shows the different hydration processes for cement samples produced by the two mixing ways. As shown in Fig. 4, the samples made by dry-mixing contain denser SEFG with much less water, and those SEFGs, including both, bonded with hydrates and not bonded, highly possibly contact each other due to much smaller voids or gaps among hydrates and SEFGs. On the other hand, in the samples made by wet-mixing, much fewer SEFG particles are wrapped and bonded in the large bulk of hydrates. Therefore, the influence of the additive, SEFGs, on the properties of the cement composite can be significant. In this experiment, the fabricated samples have small sizes, and the curing was completed. Hence, the impact of age of curing the cement composite is not considered in this experiment.

2.3. Characterization techniques

2.3.1. SEM and EDX

An SEM was used to study the morphology and distribution of the additive aggregates and cement hydrates. In contrast, EDX was used to study the concentration and distribution of different elements in the TE cement composites. The equipment adopted for SEM and EDX analyses was Hitachi S-4800 Field Emission SEM with a resolution of ~2.0 nm at 30 kV. The acceleration voltage determines the depth the electron can penetrate the sample. A higher acceleration voltage leads to more details in the deeper layer. In this case, we selected operating voltage ranging from 10 to 20 kV to observe the surface morphology of the TE cement.

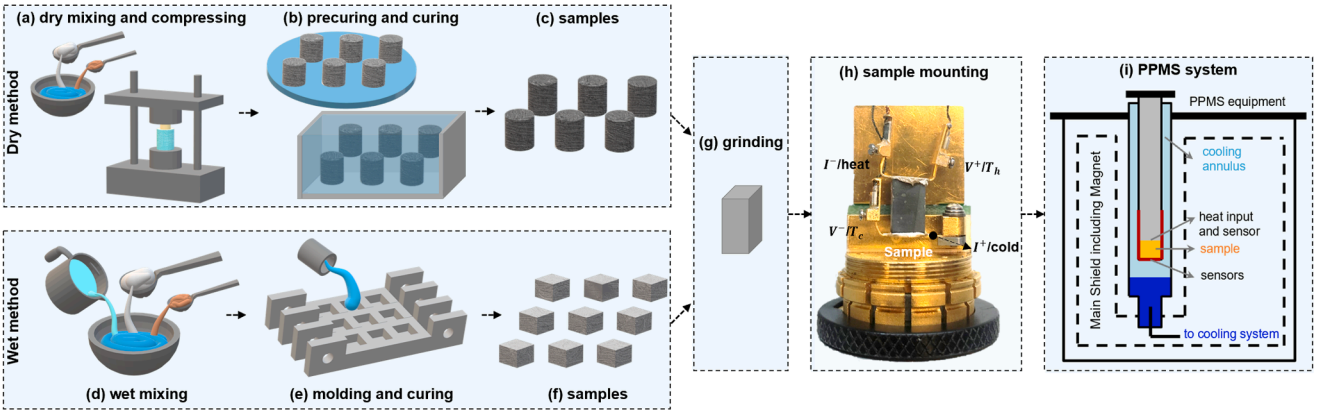

Fig. 2. The schematic diagram of the procedures for sample fabrication and property measurement: (a-c) TE cement material development via dry-mixing; (d-f) TE cement material development via wet-mixing; (g) sample grinding; (h) sample mounting and (i) PPMS testing system.

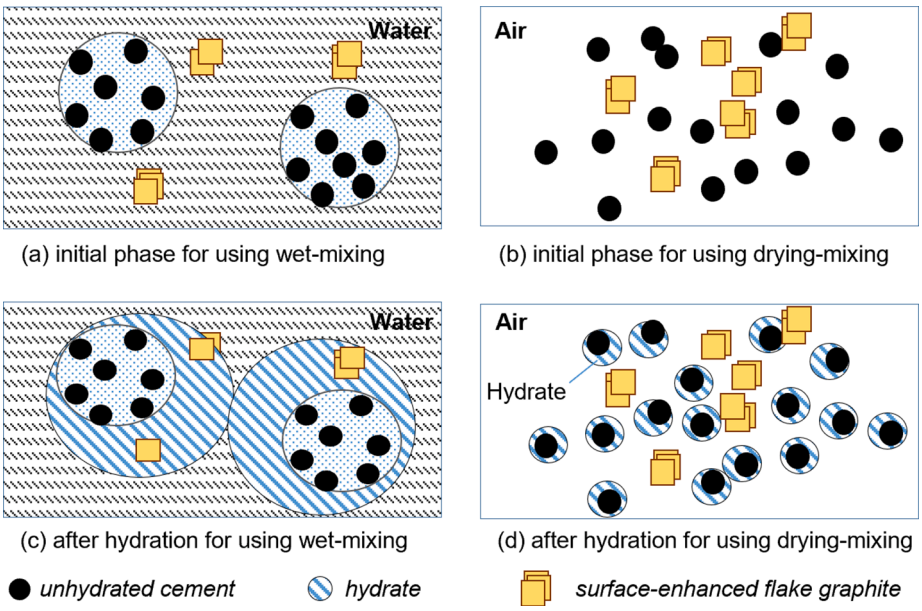

Fig. 4. Schematic illustration of hydrates for cement samples produced by wet-mixing and dry-mixing.

The magnification factor ranges from 2500 to 20,000 times. All samples were coated with a thin platinum layer for better electron drainage on the surface.

2.3.2. PPMS-TTO

We used the Thermal Transport Option (TTO) module in a DynaCool® Physical Property Measurement System (PPMS) to measure the TE properties of all TE cement composites at low temperatures (300–350 K), including the Seebeck coefficient, thermal conductivity, and electrical conductivity. Fig. 2(h) shows the puck for mounting the sample in the TTO module, and Fig. 2(i) is the schematic diagram of the PPMS. In this study, PPMS-TTO measured the thermal conductivity by the steady-state heat conduction method. It monitored the temperature gradient ($T_h - T_c$) across the sample given a known heat input through the sample. When the system achieved steady-state ($dT/dt < 0.1\%$), the thermal conductivity could be calculated based on the heat input (Q), the length (L) and area (A) of the sample, and the temperature difference across the sample (ΔT), according to Fourier's Law, as given in Eq. (1)

$$k = \frac{QL}{A\Delta T} \tag{1}$$

The influence of the convective and radiative heat loss was considered in the correction procedure. This measurement mode removes the need for extrapolating data via curve-fitting calculations and makes the results more robust. At the same time, due to the temperature gradient across the sample, the TE cement composite automatically generated a voltage output ($V^+ - V^-$). The ratio of the voltage output to the temperature gradient, both measured in real-time, is the value of the Seebeck coefficient, as expressed in Eq. (2). Cernox resistive thermometers measured the temperature gradient across the hot and cold end of the sample. The thermal voltage across the sample was measured simultaneously using a nano voltmeter.

$$S = \frac{\Delta V}{\Delta T} \tag{2}$$

After achieving steady-state and measuring the corresponding Seebeck coefficient and thermal conductivity, the system switched to the electrical conductivity measurement mode. After removing the heat source and allowing the sample to return to an isothermal state, an AC resistance bridge measured the two-probe electrical conductivity according to Ohm's Law. The operating temperature of the sample, determined by averaging T_h and T_c, was initially stabilized at 300 K before measurements and increased to 350 K with increments of 10 K during the test. Therefore, there were six tests conducted for each sample. Each trial started at a high-vacuum state of $<5 \times 10^{-4}$ torr inside the PPMS chamber.

2.3.3. PPMS-ETO

The PPMS system has the Electric Transport Option (ETO), dedicated to measuring electrical conductivity. Unlike TTO, the ETO applies the four-probe method rather than the two-probe method. This study only used ETO for exploring the difference between the two-probe and four-probe methods to measure electrical conductivity. Fig. 5 is the diagram of the test setup. The sample was placed in the electrically insulated area. Two copper wires were used to connect the two outer ends of the sample with the current input electrodes, while the other two electrodes connected were for separated voltage measurement. PPMS-ETO uses a low frequency (18–21 Hz) alternating current (AC) source with a digital lock-in with nanovolt sensitivity. The four-probe configuration separates current and voltage electrodes, eliminating the electrical resistance of the leads and contacts in the measurement, leading to a more accurate value for low-resistance samples. Although the four-probe method can provide more accurate results for low electrical resistance materials,

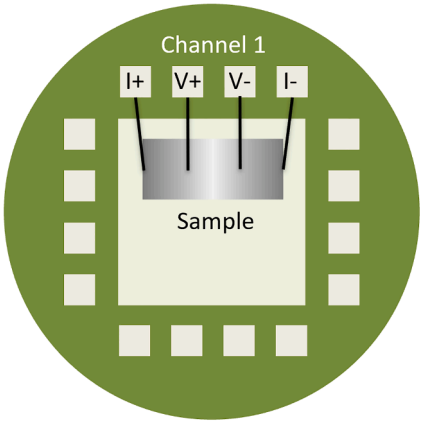

Fig. 5. Schematic diagram of the configuration of four-probe resistance measurement in PPMS-ETO.

there are difficulties inherent in applying the four-probe method in practice. Mounting four separated electrical conductive wires with a small sample is challenging.

2.4. Performance indicators

The power factor (*PF*) and the Figure of merit (*ZT*) are the two performance indicators calculated by using the three TE properties measured. The power factor is the product of the square of the Seebeck coefficient and electrical conductivity, as given in Eq. (3). The Figure of merit equals the power factor divided by the thermal conductivity, as listed in Eq. (4).

$$PF = \sigma S^2 \tag{3}$$

$$ZT = \frac{PF}{k} = \frac{\sigma S^2}{k} \tag{4}$$

2.5. Error and uncertainty analysis

PPMS system estimates the error of the measurements. The estimated error includes the random error (statistical uncertainty) and correction procedures' modeling error. The Type-A method is used to evaluate the random uncertainties by calculating the residual of the statistical distribution curve fit for the measured quantity values. In the study, the temperatures and voltages are the two directly measured quantities. There are 256 data points collected for either each temperature and or each voltage in our measurements. The data fit a normal distribution, as shown in Fig. 6. Eq. (5) and Eq. (6) are the equations to calculate the residuals of temperature and voltage. Standard deviations of the Normal distribution are the random errors of the temperature and voltage measurements.

$$R_{\Delta V} = \sqrt{\frac{\sum_i \left(\Delta V_i - \Delta V_{avg}\right)^2}{N}} \tag{5}$$

$$R_{\Delta T} = \sqrt{\frac{\sum_i \left(\Delta T_i - \Delta T_{avg}\right)^2}{N}} \tag{6}$$

The thermal conductivity, electrical conductivity, Seebeck coefficient, and *ZT* by the PPMS are from the models based on the working principles. Therefore, their errors need to use uncertainty propagation of all the involved variables, including measured variables and the others models used. The uncertainty propagation integrates the error for each variable in quadrature. The model for calculating thermal conductivity is related to the temperature measurement, heat loss to the environment, and the conductance through the shoe assemblies. Therefore, the error of the thermal conductivity,$\sigma(\kappa)$, is calculated by using Eq. (7).

$$\sigma(\kappa) = \kappa \times \sqrt{\frac{1}{N}\left(\frac{R_{\Delta T}}{\Delta T_\infty}\right)^2 + \left(\frac{P_{loss}}{P}\right)^2 + \left(\frac{0.5\Delta T_\infty K_{shoes}}{P}\right)^2} \tag{7}$$

The first term in Eq. (7) is the error of the measured temperature. The second term is the error of the thermal loss (P_{loss}) due to radiation. The P_{loss} with 100% uncertainty is related to the samples' emissivity, temperature, and surface area. The last term is the error from the conduction through the shoe assemblies, where a 50% uncertainty is assumed.

The Seebeck coefficient error, $\sigma(\alpha)$, propagates the errors of the measured voltages and temperatures (the first and second terms in Eq. (8)), and the uncertainty associated with voltage drift in the Seebeck voltage amplifier (the third term in Eq. (8)).

$$\sigma(\alpha) = \alpha \times \sqrt{\frac{1}{N}\left(\frac{R_{\Delta V}}{\Delta V_\infty}\right)^2 + \frac{1}{N}\left(\frac{R_{\Delta T}}{\Delta T_\infty}\right)^2 + \left(\frac{V_{drift}}{\Delta V_\infty}\right)^2} \tag{8}$$

The standard electrical resistivity error estimates the standard deviation of the mean of the individual resistance measurements for each resistivity measurement, which is the ratio of the measured voltage and current. As shown in Eq. (9), the total resistivity error, $\sigma(\rho)_{Total}$ is the average standard deviation of the resistance measurements ($\sigma(\rho)_1$ *and* $\sigma(\rho)_2$) on hot and cold sides.

$$\sigma(\rho)_{Total} = \frac{1}{2}\sqrt{\left[\sigma(\rho)_1\right]^2 + \left[\sigma(\rho)_2\right]^2} \tag{9}$$

The *PF* and the *ZT* errors can be obtained by propagating the error of thermal conductivity, electrical resistivity, temperature, and the Seebeck coefficient, as shown in Eqs. (10) and (11).

$$\sigma(PF) = |PF| \times \sqrt{\left(\frac{2\sigma(\alpha)}{\alpha}\right)^2 + \left(\frac{\sigma(\rho)}{\rho}\right)^2 + \left(\frac{\sigma(T)}{T}\right)^2} \tag{10}$$

$$\sigma(ZT) = |ZT| \times \sqrt{\left(\frac{2\sigma(\alpha)}{\alpha}\right)^2 + \left(\frac{\sigma(\kappa)}{\kappa}\right)^2 + \left(\frac{\sigma(\rho)}{\rho}\right)^2 + \left(\frac{\sigma(T)}{T}\right)^2} \tag{11}$$

The Type-A uncertainties of voltage and temperature were about ±0.08% and ±0.002%, respectively, under a 95.5% confidence interval. The relative estimated error, often used for comparison, is the ratio of the error estimated to the measured data. As shown in Table 1 of the summary of the relative estimated errors of the measured variables in the study, electrical resistivity has the slightest error because it only involves the directly measured voltage and current. Still, the thermal conductivity, Seebeck coefficient, *PF* have much higher errors due to the variables and assumptions used in the models for calculating them. The estimated mean error of *ZT* has the highest error of 28.4% since the ZT

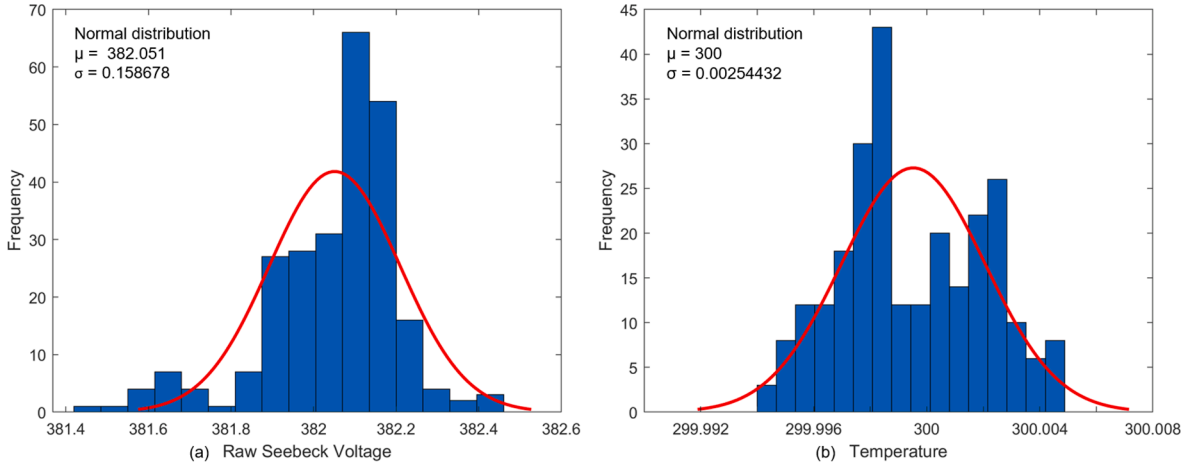

Fig. 6. Data (256 measurements) and the normal distribution of (a) raw Seebeck voltage and (b) temperature.

Table 1
Summary of relative estimated error of the five measured TE properties.

Relative estimated error	$\sigma(\kappa)/k$	$\sigma(\rho)/\rho$	$\sigma(S)/S$	$\sigma(PF)/PF$	$\sigma(ZT)/ZT$
Range	13.6%–38.5%	–	0.3%–24.6%	6.3%–34.7%	16.6%–43.3%
Mean value	23.6%	<0.01%	7.9%	13.9%	28.4%

error is the propagation of the PF and thermal conductivity errors. The literature agreed with our uncertainty analysis as seen from the published system uncertainty at 40% for a well-developed system like PPMS [30].

3. Results and analysis

3.1. Microscopic structures

The SEM images visualize the surface morphology of different TE cement composites and the distributions of additives and cement matrix. Fig. 7(a) and (b) are the SEM images of the 15SEFG/CC sample made by the dry and wet-mixing, respectively. Comparing Fig. 7(a1) and (b1), the sample made by dry-mixing (a1) has denser additives, and the sample surface is much smoother than the one made by the wet-mixing method (b1). There are some tiny cracks in the dry-mixed sample. After magnifying the gaps, the graphite and the cement appear well mixed in the cross-section of the cracks (a2). In contrast, the sample made by the wet mixing has more pores (b1 and b2). Fig. 7(b2) shows that the triangle and bright substances are the typical cement hydrate. The dark flake-shape substances located between the gaps in the cement hydrates are graphite. Fig. 7(c) includes the SEM images of the 15MnO_2/CC sample. Fig. 7(c1) shows the MnO_2 nanopowder and the cement hydrate connected as a whole piece with some internal pores. It can be observed in Fig. 7(c2) that there are aggregates of spherical particles filling in the pores of cement hydrate. They might be the MnO_2 nanopowders. Fig. 7 (d) includes the SEM images for the 5SEFG-5MnO_2/CC sample. In the sample, the cement hydrates have different shapes like stars and triangles, and the graphite looks like translucent ribbons, and the MnO_2 nanopowders are aggregated.

The EDX analysis determines the concentrations of different elements and their distributions on the surface of the sample. Fig. 8 is the collective of the EDX images of the 5MnO_2-10SEFG/CC. The spectrum at point 1 has a group of small spherical aggregate mixed with the cement hydrates. The elements with the highest concentrations are carbon, oxide, and calcium, which are three significant composites of cement powder. Compared to the spectra at point 3 and area 4, the high concentration of carbon at spectrum 1 could be the graphite. Additionally, the concentration of Mn found in this position is low. The data indicates that position one is a mixture of cement hydrates, MnO_2 powder, and graphite. Fig. 8(c) presents the spectrum at point 3, which has a typical shape of graphite flake. Carbon, oxide, and calcium still occupy the highest concentrations, but Mn did not show at this position. Fig. 8(d) presents the spectrum for the selected area in area 4, which is much larger than in points 1 and 3. It has a similar element concentration distribution, but both the concentration of oxide and Mn are higher than in points 1 and 3. The difference indicates that MnO_2 is aggregated in area 4 as compared with other points. It has been found that the larger the area scanned, the better the analysis of the elemental distribution. Since cement contains many different elements, it is challenging to detect additives with a low concentration in the cement mixture.

3.2. Thermoelectric properties

This section presents TE transport properties of SEFG-enhanced cement composites obtained from PPMS, including thermal conductivity, electrical conductivity, Seebeck coefficient, power factor, and the Figure of merit. The operating temperatures of all tests ranged from 300 K to 350 K at 10 K intervals. The experimental-data-based analysis revealed the impacts of material concentrations, fabrication methods, and adding MnO_2 in the SEFG/CC on TE performance.

3.2.1. The concentration of the additives

Fig. 9 shows how the TE transport properties of dry-mixed TE cement change with the different additive concentrations (5%, 10%, 15%) of SEFG. As seen in Fig. 9(a), the average thermal conductivity values are 2.20, 1.78, and 0.92 W/mK for 15-, 10-, and 5-SEFG/CC, respectively. The 15SEFG/CC sample has the highest thermal conductivity, while the 5SEFG/CC has the lowest. It indicates that a higher concentration of SEFG leads to higher thermal conductivity because SEFG is a highly conductive material that dramatically improves the conducive networks inside the TE cement. A higher concentration of SEFG leads to more compactly connected thermally conductive channels, resulting in higher thermal conductivity. The 15SEFG/CC sample has a higher thermal conductivity than the plain cement (0 ~ 1.6 W/mK) [31]. There is a monotonically decreasing thermal conductivity from 2.46 to 1.97 W/mK with an increase of temperature from 300 to 350 K. The thermal conductivity is a function of the motion of the free electrons in metals and semi-metal materials like SEFG. As the temperature increases, the molecular vibrations increase, decreasing the mean free path of molecules and lowering thermal conductivity.

As shown in Fig. 9(b), the electrical conductivity is also affected by the concentration of SEFG. A higher concentration causes better performance of electrical transport because SEFG introduced more free electrons. When the temperature varies from 300 to 350 K, the electrical conductivity first increases and decreases for 15- and 10-SEFG/CC, while the electrical conductivity of 5SEFG/CC remains unchanged. 15SEFG/CC sample has the highest electrical conductivity, about 121.27 S/m at 320 K. The averaged electrical conductivity values were 112.71, 102.58, and 45.12 S/m for 15-, 10-, and 5-SEFG/CC, respectively. In conclusion, SEFG can significantly increase both the thermal and electrical conductivity of the cement composite.

Fig. 9(c) is the Seebeck coefficient of SEFG-enhanced cement. The average Seebeck coefficients are 15.94, 14.99, and 11.37 μV/K for 15-, 10-, and 5-SEFG/CC, respectively. These values indicate that a high concentration of additives leads to a large Seebeck coefficient. The highest Seebeck coefficient of 16.64 μV/K is 15SEFG/CC operated at 310 K. The introduction of high-conductive SEFG improves charge carrier mobility and the change of energy barrier for increasing the Seebeck coefficient. As shown in Fig. 9(d), the power factor increases with a higher additive concentration. The average values of PF were 0.0287, 0.0231, and 0.0058 μW/(mK^2) for 15-, 10- and 5-SEFG/CCs, respectively. As shown in Fig. 9(e), 10SEFG/CC tested at 320 K and 15SEFG/CC at 330 K have the highest ZT of 4.72×10^{-6}. The ZT curve of 15SEFG/CC almost overlaps with that of 10SEFG/CC. It is due to the trade-off effect between thermal conductivity and power factor. Although 15SEFG/CC has a higher power factor, its higher thermal conductivity reduces its ZT. Meanwhile, the 5SEFG/CC sample has the lowest value of ZT. Thus, the penetration threshold of additive concentrations for improving ZT is between 10% and 15%.

3.2.2. The fabrication method

Fig. 10 compares TE transport properties of SEFG/CC samples fabricated by the dry-mixing (solid lines) and wet-mixing (dashed lines). The samples produced using the dry-mixing exhibit higher thermal and electrical conductivity than those prepared by the wet-mixing. Compared with the wet-mixed samples, the thermal conductivity improvements for dry-mixed samples are 52.2%, 35.5%, and 7.9% for 15-, 10-, and 5-SEFG/CC, respectively. The average improvements in electrical conductivity for the dry-mixed samples are 183.2%, 13266.9%, and 12504.5% for 15-, 10-, and 5-SEFG/CCs, respectively. One reason is that the sample made by conventional wet mixing contains more water content. Therefore, it has more cement hydrates than the sample made

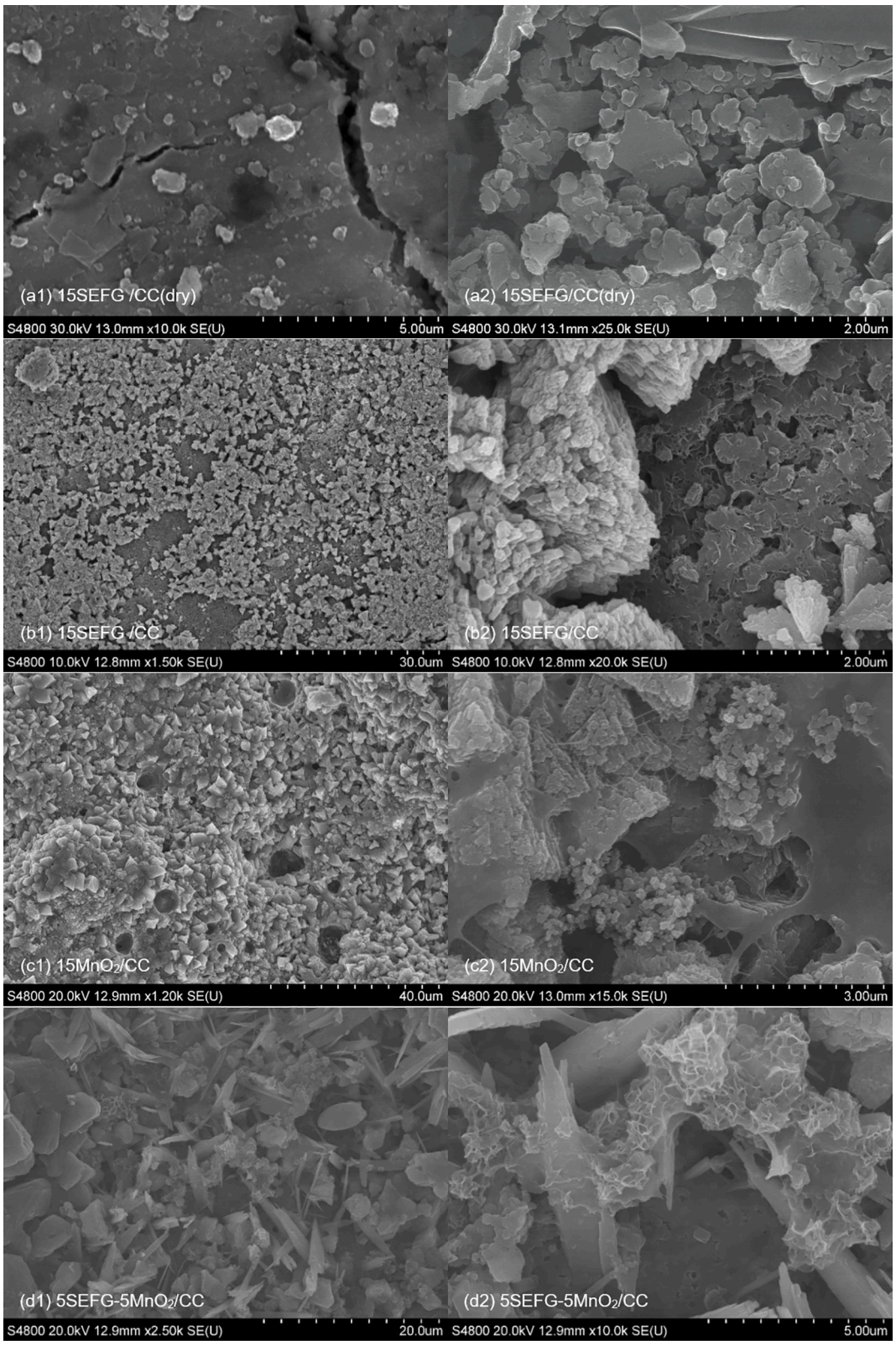

Fig. 7. The SEM images of 15SEFG/CC (dry-mixing) with a magnification of (a1) 10,000 and (a2) 25,000 times; the SEM images of 15SEFG/CC (wet-mixing) with magnifications of (b1) 1500, and (b2) 20,000 times; the SEM images of 15MnO_2/CC with magnifications of (c1) 1200, and (c2) 15,000 times; the SEM images of 5SEFG-5MnO_2/CC with magnifications of (d1) 2500 and (d2) 10,000 times.

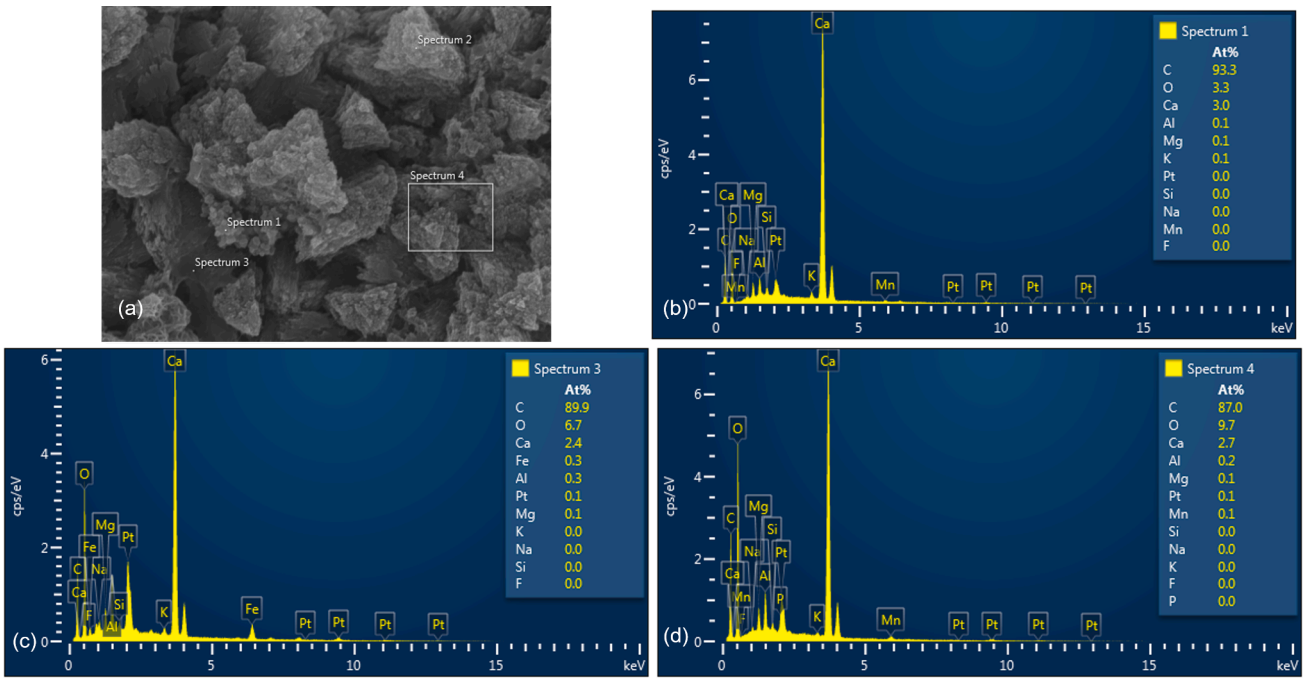

Fig. 8. (a) The SEM and EDX images of 5MnO_2-10SEFG/CC in (b) position 1 and (c) position 3 for point scanning and (d) position 4 for area scanning.

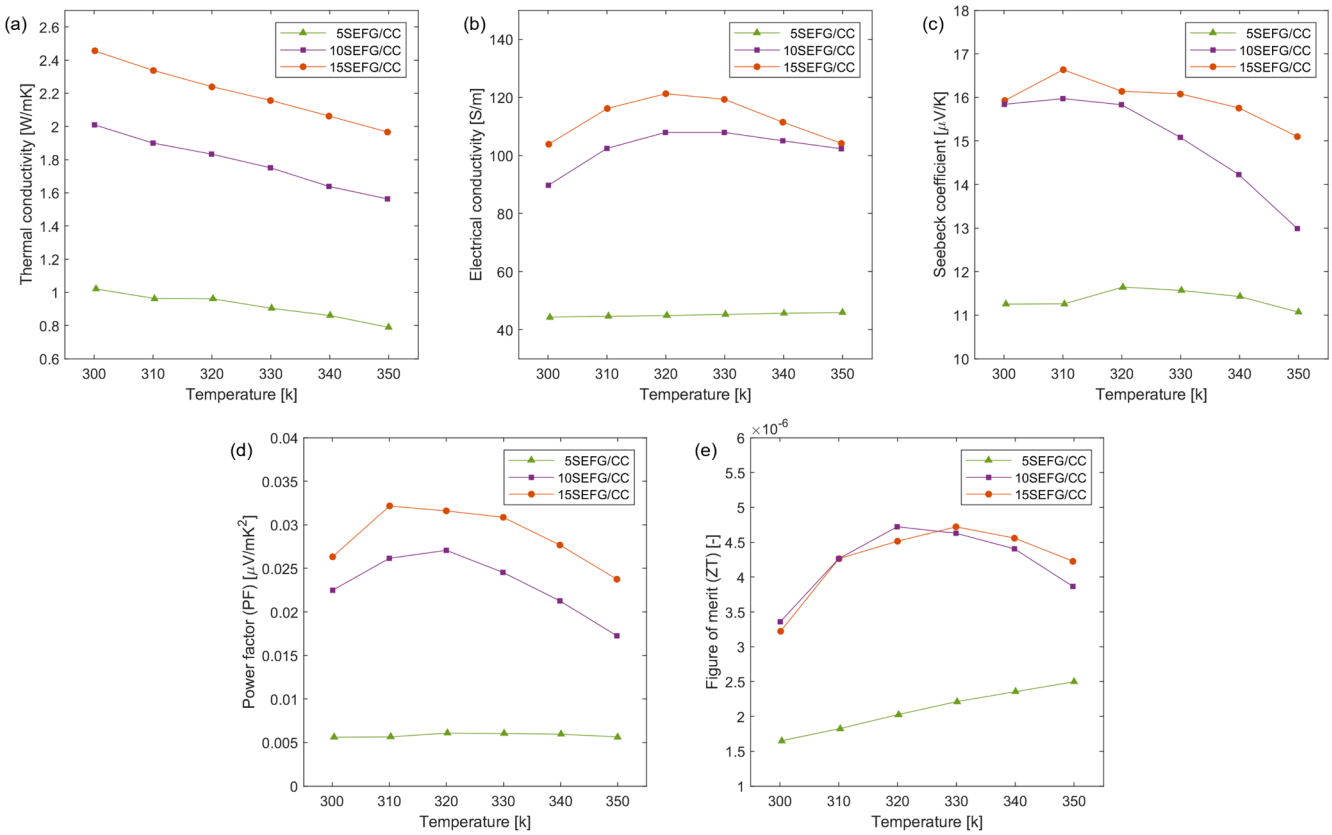

Fig. 9. The comparisons of TE transport properties of 5SEFG/CC, 10SEFG/CC, 15SEFG/CC made by the dry-mixing including (a) thermal conductivity, (b) electrical conductivity, (c) Seebeck coefficient, (d) power factor, and (e) figure of merit.

by dry mixing. Since the dry mixing applies a mechanical pressure of 50 MPa to the composite material, this compression allows the sample to contain more additives and fewer pores or voids. The additives are highly likely to contact each other, as shown in Fig. 7(a2) and (b2). In Fig. 7(b2), a large bulk of the cement hydrates (corresponding to more than 50% area of the image) appears as a group of connected bright triangle substances. There may be some graphite additives wrapped inside the bulk cement hydrates, as illustrated in Fig. 4(b). Since

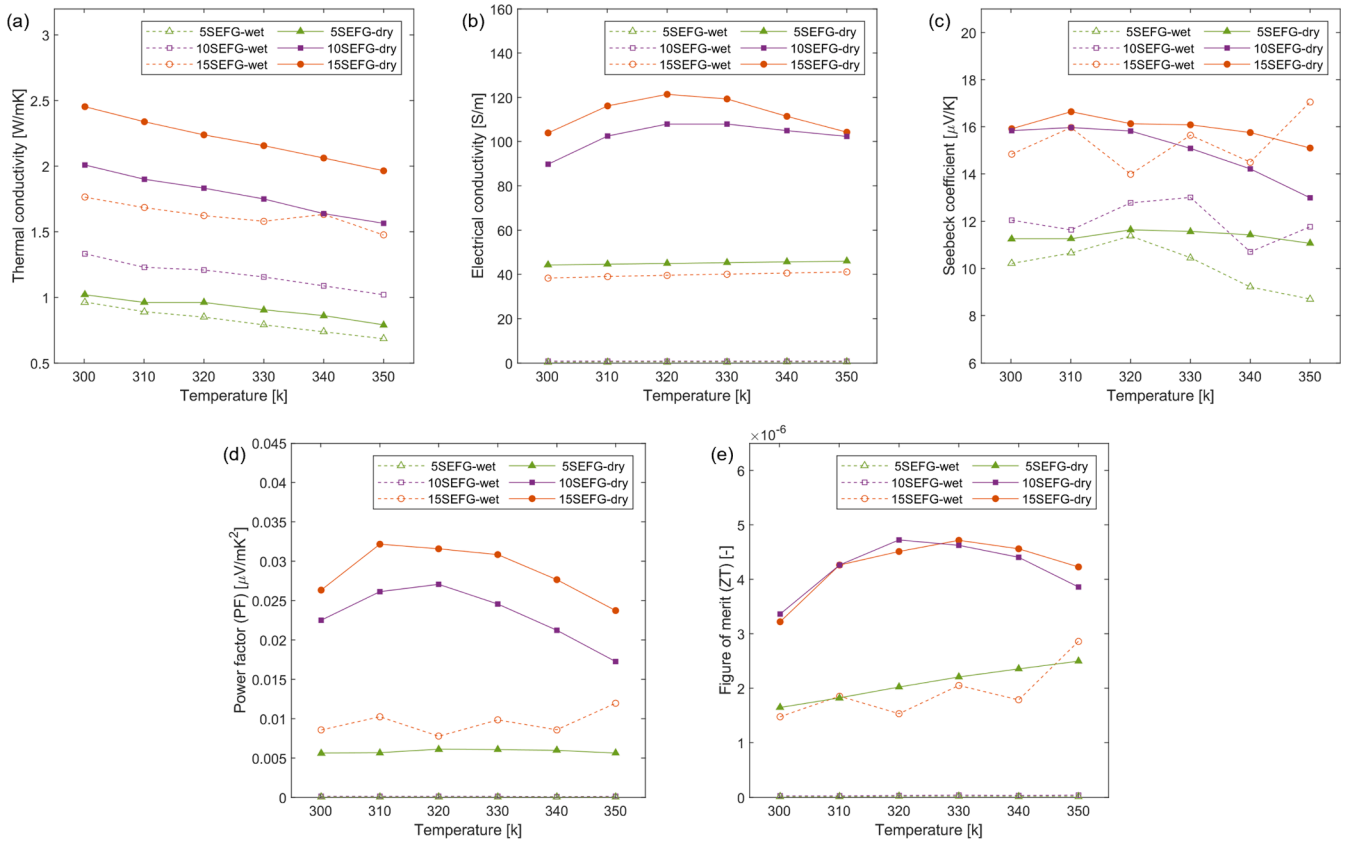

Fig. 10. The comparisons of TE transport properties of SEFG/CC made by the wet mixing and dry mixing including (a) thermal conductivity, (b) electrical conductivity, (c) Seebeck coefficient, (d) power factor, and (e) figure of merit.

additives have higher thermal and electrical conductivity than cement hydrates, the bulk cement hydrates with embedded additives reduce the potential of enhancing thermal and electric conductivity by the additives. Adjacent to the bulk cement hydrates, some loose graphites exist, as shown in the dark flake shape. On the other hand, in Fig. 7(a2), the sample made by the dry mixing has a much smaller size of aggregated cement hydrates and a more connected matrix of additives, uniformly distributed to form a more effective path for conduction. The much more connected additives improve both the thermal and electrical conductivities of thermoelectric cement composites.

The overall performance of TE material, the *ZT*, is dependent on the thermal conductivity, electrical conductivity, and the Seebeck coefficient. The dry-mixing obtains higher Seebeck coefficients of SEFG/CC than the wet mixing. As a result, comparing with wet-mixed samples, the Seebeck coefficient's improvement for dry-mixed samples were 120.4%, 13044.1%, and 19497.7% for 15-, 10-, and 5-SEFG/CC, respectively. The samples of 15SEFG/CC made by both methods and 10SEFG/CC made by the dry-mixing have the similar highest Seebeck coefficient around the value of 16 μV/K. The improvement of the Seebeck coefficient due to the increasing concentration of the additives became smaller and smaller along the concentration approaching 15%. Eventually, the samples made by the dry-mixing generally showed higher *PF* and *ZT* than those made using the wet mixing at the same additive concentration. In summary, dry mixing is a better approach to produce the TE cement composite.

The thermoelectric properties of the sample made by the dry mixing are better than those made by wet mixing. The effective medium theory and conductive network can explain this phenomenon. The thermal and electrical conductivity of the composite material highly depends on the effective network generated by the conductive additives. The sample made by the dry mixing contains a higher density of additives and allows additives contacted closely due to the high compression and exclusion of water mixing. Thus, the sample made by the dry mixing has better thermal and electrical conductivity. In addition, the slight increase in the Seebeck coefficient may be due to the refinement of its microstructure [32].

3.2.3. *The additives of MnO_2 and SEFG*

Fig. 11 compares the TE properties for 10SEFG/CC, 15SEFG/CC, and 5MnO_2-10SEFG/CC. With 5% MnO_2 powder added, the new cement composite exhibits better TE performances than either 10SEFG/CC or 15SEFG/CC. The average thermal conductivity for 5MnO_2-10SEFG/CC is 2.16 W/mK. Compared with 15SEFG/CC, 5MnO_2-10SEFG/CC has a lower thermal conductivity as the temperature is lower than 335 K and slightly higher thermal conductivity as the temperature is higher than 335 K. The reduced average thermal conductivity might be due to the different thermal conductivity of additives. The thermal conductivity of MnO_2 is around 0.1 ~ 10 W/mK, while that of the SEFG is about 100 W/mK. Compared with 10SEFG/CC, the improved thermal conductivity and electrical conductivity are due to the increased carrier concentration induced by MnO_2. According to the experimental results, the thermal conductivity of the samples continuously decreases with high temperatures. Heat in a solid is transported by lattice vibration (mainly phonons) and free electrons. With the increase in temperature, both the electric carrier and lattice vibrations increase. In the cement composite, the phonons dominate the thermal conductivity. However, phonons are effectively scattered by the imperfections, boundaries, and interfaces in the cement composite. The phonon scattering becomes more pronounced with rising temperatures. Hence, the thermal conductivity of cement composites decreases with increasing temperature.

The average electrical conductivity for 5MnO_2-10SEFG/CC is 135.83 S/m. Meanwhile, the electrical conductivity trend is very consistent in that the electrical conductivity first increases and then decreases as the temperature rises from 300 K to 350 K. The number of free carriers of

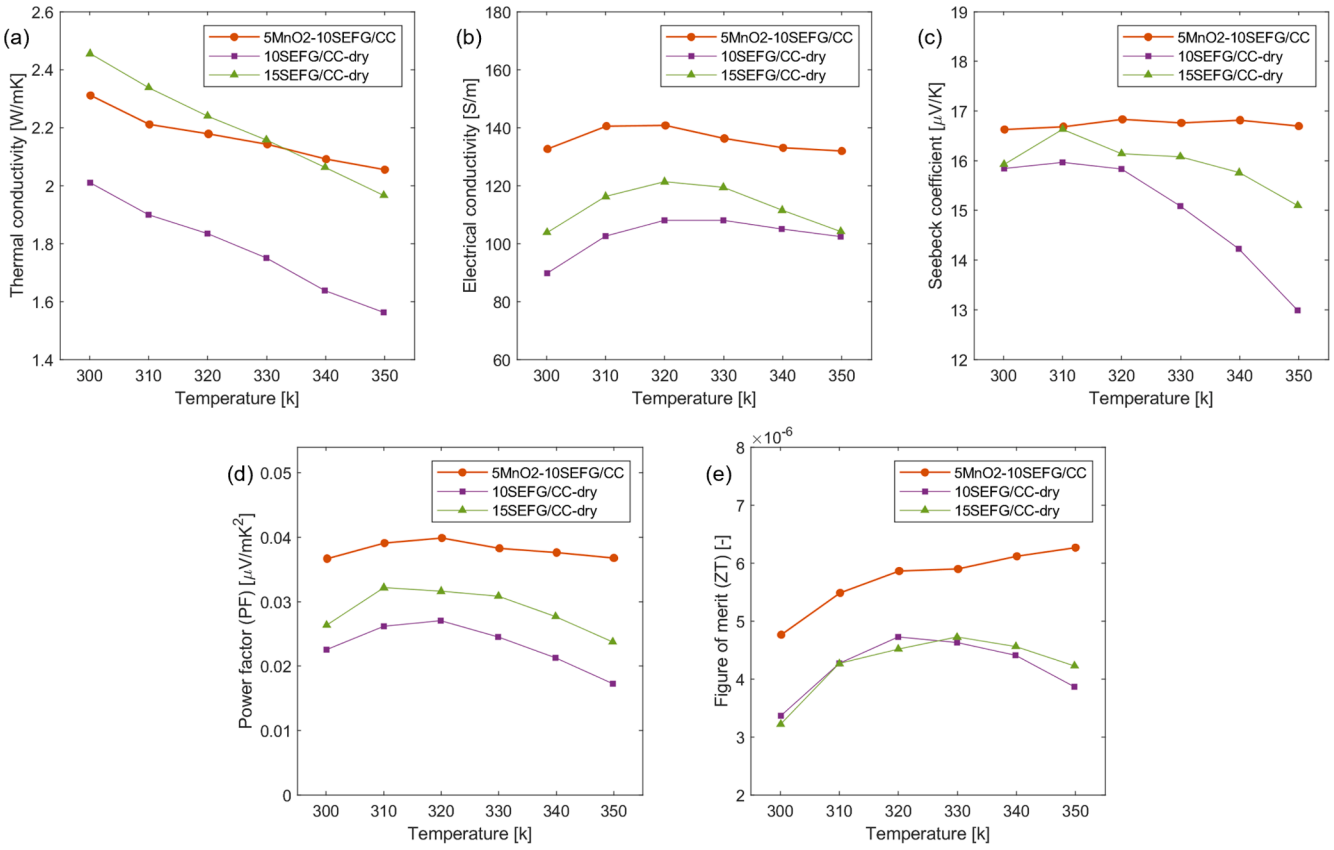

Fig. 11. The comparisons of TE transport properties of 10SEFG/CC, 15SEFG/CC, 5MnO_2-10SEFG/CC including (a) thermal conductivity, (b) electrical conductivity, (c) Seebeck coefficient, (d) power factor, and (e) figure of merit.

electric charge dominates electrical conductivity. More carriers are excited as free carriers at higher temperatures, which leads to an increase in electrical conductivity. However, the higher temperature also increases the lattice vibrations, and a more significant lattice vibration lowers the electric charge mobility. As a result, the electrical conductivity starts to decrease when the temperature is higher than 320 K.

The highest Seebeck coefficient, *PF*, and *ZT* are 16.74 μV/K, 0.0399 $\mu W/mK^2$, and 6.2×10^{-6} for 5MnO_2-10SEFG/CC, respectively. 5MnO_2-10SEFG/CC always behaves a better Seebeck coefficient, combined with a lower thermal conductivity and a higher electrical conductivity, resulting in a higher ZT. The Seebeck coefficient of SEFG-enhanced cement composites decreases at higher temperatures because the Seebeck coefficient decreases with higher carrier concentrations. However, the Seebeck coefficient of 5MnO_2-10SEFG/CC improves simultaneously and is almost constant at high temperatures due to the addition of MnO_2 nanoparticles. The Seebeck coefficient is determined by the average entropy of each charge carrier transport. Introducing an energy barrier to limit the transport of low-energy carriers while allowing high-energy carriers to pass is a strategy to increase the Seebeck coefficient without sacrificing conductivity. The nanocrystal size should approximate the carrier scattering length. A small barrier allows only higher energy carriers to pass, thus increasing the Seebeck coefficient can be obtained, and a significant barrier allows too few carriers to pass and decreases the Seebeck coefficient. Therefore, the introduction of MnO_2 nanoparticles may provide effective energy filtration to enhance the Seebeck coefficient [33,34]. As a result, the *PF* and *ZT* also improved.

3.2.4. The electrical contact resistance

This section focuses on how the two methods: two-probe and four-probe, for measuring electrical conductivity influence the measurement. In the two-probe method, the current and voltage meters are connected in parallel. The contact resistance and lead resistances are included in the resulting sample resistance. This error source becomes critical when the sample has low electrical resistance. On the other hand, the four-probe method uses the four electrodes equally spaced in a straight line on the sample. The two inner electrodes measure the electrical potential between the two internal electrodes, which are located inside the sample far from the two ending surfaces, where the contact resistance and lead resistance of the samples are, while the two outer electrodes measure the current applied to the sample. Since all the resistances are in series, the current for each sub resistance is the same and applicable for the electrical conductivity of the portion of the TE cement between the two internal electrodes. Therefore, the four-probe method gives accurate measurement by excluding the impacts from the contact and lead resistances.

We used the TTO (two-probe method) to obtain electrical conductivity for all the measured samples first. We repeated the electrical conductivity measurement for 15SEFG/CC as a study object to compare them by using the ETO (four-probe method). Fig. 12 compares the measured electrical conductivity of 15SEFG/CC obtained from two methods. The four-probe method showed ten times higher electrical conductivity than the two-probe method because it reduces the electrical contact resistance. The electrical conductivity measured by the four-probe method increases to 1040 S/m using the four-probe measurement, leading to a Figure of merit of 4.05×10^{-5} for 15SEFG/CC.

The electrical conductivity of the TE cement can be significantly different due to the differences in the additives. As seen in our study, the measured electrical conductivity ranges from 1.7×10^{-6} to 2480 S/m. Some TE cement composites behave as an insulator in electrical transport, even having capacitive properties, while others behave as metal with low resistance. Hence, the choice of the measurement method depends on the features of the samples. If the samples have low electrical resistance like graphite enhanced cement composite, the four-probe method shall be used to measure electrical conductivity accurately. On

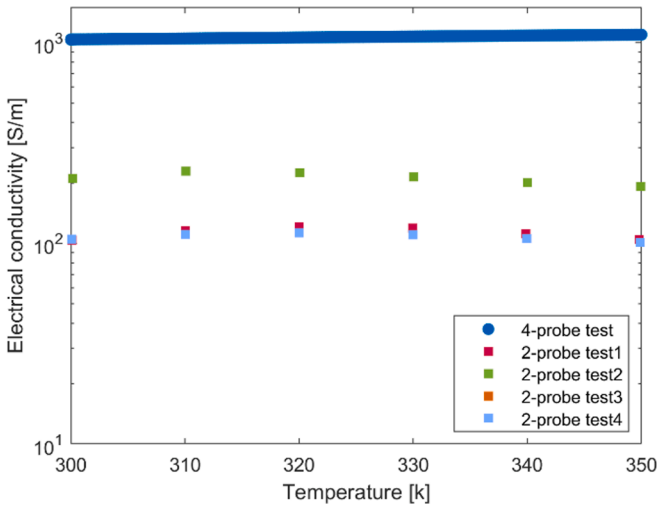

Fig. 12. Comparisons of electrical conductivity for 15SEFG/CC using the four-probe resistance measurement (blue circles) and two-probe resistance measurement (squares). (For interpretation of the references to color in this figure legend, the reader is referred to the web version of this article.)

the other hand, if the samples have a relatively high electrical resistance like carbon-fiber enhanced cement composite, the two-probe method could be used for electrical resistivity measurement with decent accuracy.

In addition, cementitious materials may have capacitive properties to hold an electrical charge. Direct current (DC) based techniques may fail to eliminate the capacitance because DC can induce high polarization effects on the electrode-concrete interface and the pore-solution-solid interface inside samples. Hence, AC is necessary to measure the electrical resistance of concrete to allow the dipole of ions in the pore solution changes its position to direct the current. The slope between measured results and the varied frequency of AC power input is the phase angle. The larger phase angle indicates a higher capacitance of the measured material. From the test result, the phase angle of 15SEFG/CC is 0.05°. This low phase angle suggests that the sample capacitance can be ignored, and sample 15SEFG/CC behaved as an ohmic resistor instead of a capacitor.

4. Conclusions

In the research, we identified and characterized the thermoelectric cement composites candidates for building envelopes. A physical property measurement system simultaneously measured the Seebeck coefficient, thermal conductivity, and electrical conductivity of the samples to study the variation of *ZT* and *PF* under different operating temperatures ranging from 300 K to 350 K. The thermoelectric performances for different concentrations of expanded graphite, different fabricating methods, the impact of MnO_2 nanopowder, and electrical contact resistance were studied and compared. The findings of the study are as follows.

A higher concentration of graphite leads to higher thermal conductivity, electrical conductivity, and the Seebeck coefficient. So is a higher *ZT*. However, when the graphite concentration is more than 10%, the Seebeck coefficient did not change significantly, and the enlarged thermal conductivity balanced the improved electrical conductivity, resulting in a similar value for *ZT*.

The fabrication method significantly influenced the results of the TE performance. Compared with wet mixing, dry mixing avoids cellulose, water reducer, or dispersants in the mixing process and allows a more effective conductive network and lower voids in cured samples. Therefore, dry-mixing is a better method for fabricating TE cement to achieve higher electrical conductivity and *ZT*.

The introduction of MnO_2 to SEFG/CC has the potential to improve TE performance. Including 5% MnO_2 powder in 10% SEFG/CC cement composite can lead to a better TE performance than 10SEFG/CC or 15SEFG/CC. The highest *ZT* (the two-probe method used), 6.2×10^{-6}, was obtained at 350 K, 36% higher than 15SEFG/CC at 330 K.

The electrical contact resistance of the sample significantly influences the measurement of electrical conductivity. The study identified the highest Figure of merit at 4.05×10^{-5} obtained for 15SEFG/CC based on the four-probe method. Therefore, the four-probe is the recommended method for measuring electrical conductivity for TE cement composites with low electrical resistance.

CRediT authorship contribution statement

Xiaoli Liu: Methodology, Investigation, Writing - original draft. **Ming Qu:** Supervision, Conceptualization, Funding acquisition, Writing - review & editing. **Alan Phong Tran Nguyen:** Investigation. **Neil R. Dilley:** Methodology, Writing - review & editing. **Kazuaki Yazawa:** Methodology, Writing - review & editing.

Declaration of Competing Interest

The authors declare that they have no known competing financial interests or personal relationships that could have appeared to influence the work reported in this paper.

Acknowledgments

This material is based upon work supported by the National Science Foundation under Grant No. CBET-1805818.

References

[1] M. Hasebe, Y. Kamikawa, S. Meiarashi, Thermoelectric generators using solar thermal energy in heated road pavement, in: 2006 25th Int. Conf. Thermoelectr., IEEE; 2006, pp. 697–700. 10.1109/ict.2006.331237.
[2] S.A. Tahami, M. Gholikhani, R. Nasouri, S. Dessouky, A.T. Papagiannakis, Developing a new thermoelectric approach for energy harvesting from asphalt pavements, Appl. Energy 238 (2019) 786–795, https://doi.org/10.1016/j.apenergy.2019.01.152.
[3] W. Jiang, J. Xiao, D. Yuan, H. Lu, S. Xu, Y. Huang, Design and experiment of thermoelectric asphalt pavements with power-generation and temperature-reduction functions, Energy Build. 169 (2018) 39–47, https://doi.org/10.1016/j.enbuild.2018.03.049.
[4] U. Datta, S. Dessouky, A.T. Papagiannakis, Harvesting thermoelectric energy from asphalt pavements, Transp. Res. Rec. J. Transp. Res. Board 2628 (2017) 12–22, https://doi.org/10.3141/2628-02.
[5] W. Jiang, D. Yuan, S. Xu, H. Hu, J. Xiao, A. Sha, Y. Huang, Energy harvesting from asphalt pavement using thermoelectric technology, Appl. Energy 205 (2017) 941–950, https://doi.org/10.1016/j.apenergy.2017.08.091.
[6] R.A. Khire, A. Messac, S. Van Dessel, Design of thermoelectric heat pump unit for active building envelope systems, Int. J. Heat Mass Transf. 48 (2005) 4028–4040, https://doi.org/10.1016/j.ijheatmasstransfer.2005.04.028.
[7] Z. Liu, L. Zhang, G. Gong, Y. Luo, F. Meng, Evaluation of a prototype active solar thermoelectric radiant wall system in winter conditions, Appl. Therm. Eng. 89 (2015) 36–43, https://doi.org/10.1016/j.applthermaleng.2015.05.076.
[8] Z. Liu, L. Zhang, G. Gong, T. Han, Experimental evaluation of an active solar thermoelectric radiant wall system, Energy Convers Manag 94 (2015) 253–260, https://doi.org/10.1016/j.enconman.2015.01.077.
[9] Z.B. Liu, L. Zhang, G. Gong, Y. Luo, F. Meng, Experimental study and performance analysis of a solar thermoelectric air conditioner with hot water supply, Energy Build. 86 (2015) 619–625, https://doi.org/10.1016/j.enbuild.2014.10.053.
[10] M. Ibañez-Puy, C. Martín-Gómez, J. Bermejo-Busto, J.A. Sacristán, E. Ibañez-Puy, Ventilated Active Thermoelectric Envelope (VATE): Analysis of its energy performance when integrated in a building, Energy Build. 158 (2018) 1586–1592, https://doi.org/10.1016/j.enbuild.2017.11.037.
[11] K. Irshad, K. Habib, N. Thirumalaiswamy, B.B. Saha, Performance analysis of a thermoelectric air duct system for energy-efficient buildings, Energy 91 (2015) 1009–1017, https://doi.org/10.1016/j.energy.2015.08.102.
[12] W. He, G. Zhang, X. Zhang, J. Ji, G. Li, X. Zhao, Recent development and application of thermoelectric generator and cooler, Appl. Energy 143 (2015) 1–25, https://doi.org/10.1016/j.apenergy.2014.12.075.
[13] X. Liu, R. Jani, E. Orisakwe, C. Johnston, P. Chudzinski, M. Qu, B. Norton, N. Holmes, J. Kohanoff, L. Stella, H. Yin, K. Yazawa, State of the art in composition, fabrication, characterization, and modeling methods of cement-based

thermoelectric materials for low-temperature applications, Renew. Sustain. Energy Rev. 137 (2021) 110361, https://doi.org/10.1016/j.rser.2020.110361.
[14] M. Sun, Z. Li, Q. Mao, D. Shen, Thermoelectric percolation phenomena in carbon fiber-reinforced concrete, Cem. Concr. Res. 28 (1998) 1707–1712, https://doi.org/10.1016/S0008-8846(98)00161-6.
[15] M. Sun, Z. Li, Q. Mao, D. Shen, Study on the hole conduction phenomenon in carbon fiber-reinforced concrete, Cem. Concr. Res. 28 (1998) 549–554, https://doi.org/10.1016/S0008-8846(98)00011-8.
[16] D. Bahar, Y. Salih, Thermoelectric behavior of carbon fiber reinforced lightweight concrete with mineral admixtures, New Carbon Mater. 23 (2008) 21–24, https://doi.org/10.1016/S1872-5805(08)60009-8.
[17] J. Wei, Z. Nie, G. He, L. Hao, L. Zhao, Q. Zhang, Energy harvesting from solar irradiation in cities using the thermoelectric behavior of carbon fiber reinforced cement composites, RSC Adv. 4 (2014) 48128–48134, https://doi.org/10.1039/C4RA07864K.
[18] J. Wei, L. Zhao, Q. Zhang, Z. Nie, L. Hao, Enhanced thermoelectric properties of cement-based composites with expanded graphite for climate adaptation and large-scale energy harvesting, Energy Build. 159 (2018) 66–74, https://doi.org/10.1016/j.enbuild.2017.10.032.
[19] S. Ghosh, S. Harish, K.A. Rocky, M. Ohtaki, B.B. Saha, Graphene enhanced thermoelectric properties of cement based composites for building energy harvesting, Energy Build. 202 (2019) 109419, https://doi.org/10.1016/j.enbuild.2019.109419.
[20] S. Ghosh, S. Harish, M. Ohtaki, B.B. Saha, Enhanced figure of merit of cement composites with graphene and ZnO nanoinclusions for efficient energy harvesting in buildings, Energy 198 (2020) 117396, https://doi.org/10.1016/j.energy.2020.117396.
[21] J. Wei, Y. Fan, L. Zhao, F. Xue, L. Hao, Q. Zhang, Thermoelectric properties of carbon nanotube reinforced cement-based composites fabricated by compression shear, Ceram. Int. 44 (2018) 5829–5833, https://doi.org/10.1016/j.ceramint.2018.01.074.
[22] L. Tzounis, M. Liebscher, R. Fuge, A. Leonhardt, V. Mechtcherine, P- and n-type thermoelectric cement composites with CVD grown p- and n-doped carbon nanotubes: Demonstration of a structural thermoelectric generator, Energy Build. 191 (2019) 151–163, https://doi.org/10.1016/j.enbuild.2019.03.027.
[23] S. Wen, D.D.L. Chung, Seebeck effect in steel fiber reinforced cement, Cem. Concr. Res. 30 (2000) 661–664, https://doi.org/10.1016/S0008-8846(00)00205-2.
[24] J. Wei, L. Hao, G.P. He, C.L. Yang, Thermoelectric power of carbon fiber reinforced cement composites enhanced by Ca3Co4O9, Appl Mech Mater 320 (2013) 354–357, https://doi.org/10.4028/www.scientific.net/amm.320.354.
[25] J. Wei, L. Hao, G. He, C. Yang, Enhanced thermoelectric effect of carbon fiber reinforced cement composites by metallic oxide/cement interface, Ceram. Int. 40 (2014) 8261–8263, https://doi.org/10.1016/j.ceramint.2014.01.024.
[26] T. Ji, X. Zhang, W. Li, Enhanced thermoelectric effect of cement composite by addition of metallic oxide nanopowders for energy harvesting in buildings, Constr. Build. Mater. 115 (2016) 576–581, https://doi.org/10.1016/j.conbuildmat.2016.04.035.
[27] S. Ghahari, E. Ghafari, N. Lu, Effect of ZnO nanoparticles on thermoelectric properties of cement composite for waste heat harvesting, Constr. Build. Mater. 146 (2017) 755–763, https://doi.org/10.1016/j.conbuildmat.2017.04.165.
[28] S. Wen, D.D.L. Chung, Enhancing the Seebeck effect in carbon fiber-reinforced cement by using intercalated carbon fibers, Cem. Concr. Res. 30 (2000) 1295–1298, https://doi.org/10.1016/S0008-8846(00)00341-0.
[29] D.P. Bentz, Blending different fineness cements to engineer the properties of cement-based materials n.d. 10.1680/macr.2008.62.5.327.
[30] J.D. König, A. Jacquot, H.-F. Pernau, J. König, U. Nussel, M. Bartel, et al. Measurement uncertainties in thermoelectric research. 8th Eur. Conf. Thermoelectr., Como: 2010, p. 1–11. <https://www.researchgate.net/publication/291295184 (accessed March 17, 2021).
[31] M. Hajmohammadian Baghban, P.J. Hovde, S. Jacobsen, Analytical and experimental study on thermal conductivity of hardened cement pastes, Mater. Struct. Constr. 46 (2013) 1537–1546, https://doi.org/10.1617/s11527-012-9995-y.
[32] D. Li, X.Y. Qin, H.J. Li, J. Zhang, H.H. Hoon, The effects of high-pressure compression on transport and thermoelectric properties of TiS2 at low temperatures from 5 to 310 K, J. Appl. Phys. 103 (2008) 123704, https://doi.org/10.1063/1.2938748.
[33] J. Martin, L. Wang, L. Chen, G.S. Nolas, Enhanced Seebeck coefficient through energy-barrier scattering in PbTe nanocomposites, Phys. Rev. B – Condens. Matter. Mater. Phys. 79 (2009), 115311, https://doi.org/10.1103/physrevb.79.115311.
[34] J. Hu, B. Liu, H. Subramanyan, B. Li, J. Zhou, J. Liu, Enhanced thermoelectric properties through minority carriers blocking in nanocomposites, J. Appl. Phys. 126 (2019) 095107, https://doi.org/10.1063/1.5118981.